# Study of damage evolution in 316L stainless steel composite enamel coatings by in situ scanning electron microscopy and acoustic emissions analyses

Francesca Russo [a,*], Emiliano Rustighi [a], Radek Mušálek [b], Tomáš Tesař [b], Vigilio Fontanari [a], Stefano Rossi [a]

[a] *Department of Industrial Engineering, University of Trento, Via Sommarive 9, 38123 Trento (TN), Italy*
[b] *Department of Materials Engineering, Institute of Plasma Physics of the Czech Academy of Sciences, Za Slovankou 1782/3, 18200 Prague 8, Czech Republic*

ABSTRACT

Ceramics and glass ceramics are used in many demanding applications due to their exceptional properties including wear resistance, thermal stability, and corrosion resistance. However, sizable efforts are spent to improve their low fracture toughness, by, for example, modification of microstructure, and fiber-reinforcement. The addition of metallic particles also represents a well-known approach to solve this issue. Metal-reinforced glass-ceramics also emerge as a potential solution providing the desirable ability of crack bridging and absorption of energy by ductile deformation. This concept was in this study applied to the production of novel composite enamel coatings with different amount of 316L stainless steel flakes. This study aims to evaluate the steel-enamel composite coatings' mechanical properties, using flexural tests and in-situ techniques. Acoustic Emission is introduced as a valuable method to monitor damage evolution and the quantitative results are compared to combined SEM in-situ flexural tests carried out on the same samples. The addition of stainless-steel flakes resulted to effectively counteract the nucleation and propagation of cracks and the AE technique was demonstrated to be a first-choice method for assessing the mechanical properties of composite enamel coatings.

## 1. Introduction

Ceramics and glass ceramics have become the materials of choice in many demanding applications, including tribological components, automotive engines, aerospace vehicles, and power generators, as they display superior wear resistance, thermochemical stability, remarkable hardness, and excellent resistance to corrosive environments [1–3]. However, these exceptional properties are offset by a significant drawback: low toughness. Toughness is an essential characteristic for materials subjected to mechanical and thermal stresses; for this reason, it is important to improve the mechanical properties of these materials, and many different strategies can be adopted. It is for example possible to modify the internal microstructure, develop transformation-toughening materials, such as transformation-toughened zirconia (TTZ), create whisker-reinforced [4] or fiber-reinforced ceramics [5–7], and design cermets materials (ceramic and metal compounds) [8].

Cermets are renowned for their high toughness and extremely high strength as they show ductility reinforcement, whereas fiber-reinforced ceramics show impressive fracture energies, as the presence of ceramic fibers guarantees the development of crack bridging mechanisms [9].

Thus, a possible solution to combine the effect of fibers (ability to bridge an advancing crack) with ductility (ability to absorb mechanical energy without failure) is to create metal-reinforced ceramics [10–13], where several toughening mechanisms may operate together. Multiple examples of metal-reinforced ceramic matrix composites are reported in the literature, such as $Al_2O_3$ based composites with Ni [14,15], Al [16, 17], Mo [18], $ZrO_2$ based materials [19], and hydroxyapatite-based composites for biomedical applications [20]. Metallic particle toughening has also proven effective with glass-matrix composites, as reported by several literature studies [21–25].

In this context, it is interesting to exploit this toughening approach to improve the mechanical properties also of vitreous enamel coatings. Vitreous enamels are silica-based inorganic coatings deposited on steel and aluminium alloys substrates by high-temperature vitrification [26, 27]. These coatings are mainly appreciated for their ability to withstand degradation by external weathering agents and corrosive environments,

and they show excellent resistance to thermal shocks, chemicals, and mild-abrasive phenomena [28–33]. Though enamels show good hardness, they have limited mechanical properties due to the brittle behaviour of the glassy matrix, and the application of mechanical stresses can lead to the development of through-thickness cracks and thus to a decreased durability of the enamelled components.

The addition of metallic particles inside the enamel matrix was proven to have a positive effect on abrasion resistance, thermal shock resistance, and self-healing properties [34,35]. Many examples regarding the use of steel additives as a second phase in ceramic and glass-based composites can be easily found in the literature [36–38], and recent studies have demonstrated that the addition of 316L stainless steel flakes inside the enamel matrix is able to improve the abrasion resistance and the cracking resistance of these coatings, without serious negative side effects [39].

The present study will focus on the assessment mechanical properties of composite steel/enamel coatings by flexural tests coupled with in-situ techniques.

The targeted characterization of enamel's mechanical properties can be very challenging due to the small thickness of the coatings, presence of residual stresses [40], and testing complexity. Short crack techniques, such as the indentation fracture method, can offer a qualitative understanding of the coating's toughness, but they include strong limitation on porous coatings. On the other hand, long crack methods are difficult to implement due to the complexity involved in preparing sharp pre-cracks especially for thin layers [41]. In this context, it is possible to combine flexural tests with in-situ SEM observations or Acoustic Emission (AE) analyses to quantitatively assess the cracking resistance of the coatings and understand the additive-crack interaction phenomena [42, 43].

Acoustic Emission (AE) is a well-established NDT&E (non-destructive testing and evaluation) method [44] to monitor damage evolution in composite polymeric [45–48], ceramic-matrix [49–52], and metallic materials [53–55], as it is able to detect the occurrence of damage at low-stress condition that does not provide a visible effects on the tensile stress strain curve. The activity (i.e., number of acoustic events) and parametric (i.e., amplitude and energy of acoustic events) analysis of the AE pattern can provide valuable information about a wide range of structural failures [56]. The interpretation of the signals, and hence establishing of a relationship between a specific failure mode and its acoustic signature is however still a challenge and a concurrent in-situ SEM analysis could provide deeper insights. In this context, there is a lack of literature that thoroughly examines the behaviour of composite enamel coatings using in-situ techniques. Specifically, the benefits of the AE technique for understanding the role of additives in enamel formulations have not been previously evaluated. Therefore, this study aims to emphasize the value of combining experimental techniques, such as in-situ SEM and AE, to investigate the mechanical behaviour of vitreous enamel coatings.

This study aims to assess the mechanical properties of composite vitreous enamel coatings fabricated with the addition of 316L stainless steel flakes in 1 wt% and 5 wt% concentration by means of in-situ techniques. First, an experimental assessment of post-firing residual stresses will be exploited. Subsequently, in-situ 3-point and 4-point flexural tests will be carried out with coupling SEM observations. The results of in-situ AE tests during 4-point flexural tests will be discussed

and the main positive and negative features of this tests will be highlighted, giving new perspectives on the mechanical analysis of enamel coatings.

## 2. Materials and experimental method

### 2.1. Coatings deposition

AA5005 aluminium alloy panels measuring 120 mm $\times$ 20 mm x 1.5 mm were used as substrates. To ensure good adhesion of the enamel on the substrate, the panels were chemically pretreated according to the following procedure: immersion in acetone for 2 min using an ultrasound bath, water rinsing, immersion in a 10 w/v % NaOH aqueous solution for 5 min at room temperature, water rinsing, immersion in a 25 v/v % HNO$_3$ aqueous solution for 20 s at room temperature, water rinsing, and drying with compressed air. At the end of this procedure, the average surface roughness parameter (Ra) of the aluminum substrate was equal to 0.62 $\pm$ 0.09 μm, with an increase of 2.5 times with respect to the pristine state.

The samples were deposited using a vanadium-based ready-to-use (RTU) frit, developed by Emaylum Italia (Chignolo d'Isola, BG, Italy). The frit's compositional analysis revealed a significant amount of sodium and magnesium oxides, accounting for approximately 29 % of its content. This high concentration of alkali oxides was necessary to reduce the softening temperature of the frit below 580 °C [57].

A cobalt aluminate blue spinel (CoAl$_2$O$_4$) commercial pigment was used to obtain opaque blue enamel coatings. The 316L stainless-steel flakes (SS–F) used in this study are commercial non-leafing pigments (STAY/STEEL 316L K, Eckart Hartenstein, Germany). Further details on the technical specifications of the frit and the metallic additive are reported in previous studies [34].

The three different components (frit, pigment, and stainless steel flakes) were mixed to obtain one reference formulation (without SS-F) and two composite formulations, according to the ratios reported in Table 1.

The quantity of the 316 SS-F additive represents the 1 wt% and 5 wt % of the total powder content of the 1 % SS-F and 5 % SS-F formulations, respectively. The mixed powders were suspended in a water-borne screen-printing medium to obtain an applicable screen-printing paste, that was passed through a three-cylinder refiner to obtain a uniform dispersion of the SS-F additive into the application medium. The samples were deposited using an 18-wire screen-printing mask and exploiting a 2A/1F (2 applications/1 firing) cycle, consisting of two applications followed by drying steps at 200 °C for 15 min and a firing step at 570 °C for 15 min in a static muffle furnace.

### 2.2. Samples characterization

The coating thickness was measured using a Phynix Surfix FN thickness gauge and exploiting 30 measurements on 3 different samples for each sample series. The surface roughness was assessed using a MAHR Marsurf PS1 roughness tester. A sampling length (l$_r$) of 0.8 mm and an evaluation length (l$_n$) of 5.6 mm were used according to the UNI EN ISO 4288 (2000) standard. The reported values R$_a$ (arithmetic average of the roughness profile) and R$_z$ (average roughness depth) are the average of 15 measurements carried out on three different samples

**Table 1**
Composition of the enamel formulations under investigation.

| COMPONENT | REFERENCE FORMULATION | 1 % SS-F FORMULATION | 5 % SS-F FORMULATION |
|---|---|---|---|
| **RTU frit** | 85 g | 84.15 g | 80.75 g |
| **CoAl$_2$O$_4$ pigment** | 15 g | 14.85 g | 14.25 g |
| **316L SS-F** | – | 1 g | 5 g |
| **Total powder** | 100 g | 100 g | 100 g |
| **Printing medium** | 45 g | 45 g | 45 g |

(5 measures each). Optical (Nikon SMZ25, Nikon, Tokyo, Japan) and scanning electron microscope (SEM) (Zeiss Evo MA15, Zeiss, Oberkochen, Germany) were used to evaluate the distribution of the filler in the coating and assess the coating's internal microstructure. The samples were saw-cut and the cross-sections were grinded and polished until a 1 μm diamond paste. The evaluation of porosity was addressed using the ImageJ software, the reported values are the average of three measurements on different samples.

## 2.3. Experimental residual stress evaluation by thermal analysis

The coupling of enamel and aluminum, which have different thermal behaviors, results in the onset of residual stresses in the composite system. These residual stresses (in enamel coatings these stresses are compressive type) can influence the mechanical behavior of the coatings by delaying the occurrence of first crack. By assuming macroscopically homogeneous and isotropic materials, researchers can determine these residual stresses using a combination of optical dilatometric and optical flexure analyses, as previously described in the literature [58,59].

Dilatometric analyses were exploited on prismatic samples (reference, 1 % SS-F, and 5 % SS-F) having dimensions of 50 mm × 5 mm x 5 mm. Dry formulations (5 g) were mixed with water (0.5 g), compacted in a die, dried at 90 °C for 30 min, and fired at 570 °C for 15 min, increasing the furnace temperature at a rate of 80 °C/min. The dilatometric analyses were carried out using the ELS-MDF horizontal optical dilatometer (Expert Lab Service, Modena, Italy) with a heating rate of 5 °C/min and a maximum temperature of 570 °C. The aluminum substrate was tested by exploiting the same thermal cycle. No-load flexural analyses were carried out using the ELS-MDF optical fleximeter (Expert Lab Service, Modena, Italy) with a heating rate of 5 °C/min and a maximum temperature of 570 °C. The samples for the no-load flexural analyses were saw-cut to obtain samples with dimensions of 85 mm × 10 mm x 1.6 mm.

## 2.4. Preliminary evaluation of substrate's mechanical properties

A preliminary evaluation of the substrate's mechanical properties is carried out to identify its Young's modulus and yield stress. The metallic samples were heat-treated (heating at 200 °C 15 min, cooling at RT, heating at 200 °C 15 min, and heating at 570 °C for 15 min) to resemble the condition existing after enamel firing. Three tensile tests were performed on a UTM Instron 8516 machine (Instron, Glenview, USA) at a test speed of 0.5 mm/min. The elastic modulus was determined to be $71.7 \pm 3.7$ GPa, and the tensile yield stress (calculated using the 0.2 % method) was found to be $49.5 \pm 8.5$ MPa. These measurements provided valuable information for identifying the elastic/plastic limit of stress-strain curves obtained during 3-point and 4-point bending tests.

## 2.5. In-situ 3-point and 4-point flexural tests with microtest deben tensile tester

Samples were saw-cut to obtain enamelled strips with dimensions of 2.5 mm × 30 mm x 1.6 mm, after that the cross-sections were polished up to 1 μm diamond suspension. The samples were tested with an instrumented in-situ Microtest 200 N tensile tester (Deben, Suffolk, UK) mounted on a Zeiss EVO MA15 (Zeiss, Oberkochen, Germany) scanning electron microscope, that was operated in low-vacuum mode (30 Pa). The tests were both performed in three-point (3 PB) and four-point (4 PB) bending configuration in position control with a testing speed of 0.2 mm/min up to 1 mm displacement. A preload of 0.5 N was applied prior to testing and displacement was stopped at regular intervals to acquire SEM micrographs of the damaged coatings. The supports used in the tests had a diameter of 3.94 mm, and the outer support span was equal to 23 mm; in the case of four-point bending tests the loading span was equal to 6 mm. The loading support/supports were in contact with the substrate so that crack initiation on the coating side of the sample was

ensured and the coating was tested in tension.

## 2.6. In-situ AE tests in four-point bending setup (UTM)

Acoustic Emission (AE) measurements were conducted on samples having dimensions of 20 mm × 60 mm x 1.6 mm. The 4-point bending tests were performed using a Tinius Olsen H10KT universal testing machine (Tinius Olsen, Horsham, UK) equipped with a 5 kN load cell and operated at a cross-head displacement rate of 0.2 mm/min. The coatings were tested in tension and the tests were stopped when reaching a displacement of 2 mm and. The support span was equal to 30 mm and the loading span was equal to 10 mm (1/3-1/3-1/3 configuration).

A Mistras 1283 AE USB node AE equipment was utilized to record the AE signals. The AE signals were detected by a transducer (Model PICO 80, Mistras, Princetown Junction, USA) placed on the coating outside the support span area. The threshold value for the AE measurements was set at 40 dB, and the frequency range for acquisition was set between 20 kHz and 1 MHz. Three samples were tested for each coating formulation. The bare substrate was also tested in order to assess its acoustic pattern. An activity and a parametric analysis were performed on the acquired measurements.

## 3. Results and discussion

### 3.1. Samples characterization

Table 2 displays the thickness and surface roughness results. The addition of a small amount of stainless-steel additive has no noticeable effect on the topography of the sample. However, when a higher quantity of flakes is introduced, it adversely affects the smoothness of the coating's surface, leading to a significant increase in roughness, approximately by a factor 600 %. Thus, the presence of a high concentration of SS-Fs has a non-negligible effect on the sintering behaviour of the composite formulation, hindering the creation of a smooth surface [39]. This effect is probably due to changes in thermal behaviour of the formulation caused by the presence of the metallic flakes, and it is highlighted in the finished products as the firing parameters have been kept the same for all the samples.

Fig. 1 (a-c) shows in plane optical images of the sample's surfaces. Fig. 1 (d-f) shows cross-sectional SEM images of the sample's microstructure. The dispersion of stainless-steel flakes within the matrix is uniform, and there are no noticeable agglomeration phenomena. All the samples show the presence of a closed-porosity structure, which is a typical feature of enamel coatings arising from gas evolution during firing. Table 2 provides an assessment of the porosity level for the samples under investigation. Considering the experimental error, no significant differences are observed in the maximum pore diameter, but a great variation in the total internal porosity is evident. This difference could be attributed to three factors: incomplete densification of the frit particles during firing, preferential nucleation of bubbles at heterogeneous interfaces, and trapping of bubbles in a viscous formulation. The increase in porosity corresponds with an increase in surface roughness. In this context, a high quantity of metallic additive seems to hinder the complete densification of frit particles, resulting in a rougher and more porous coating.

As regards the stainless-steel flakes, they do not assume a preferred

**Table 2**
Topographical and microstructural parameters of the samples under study.

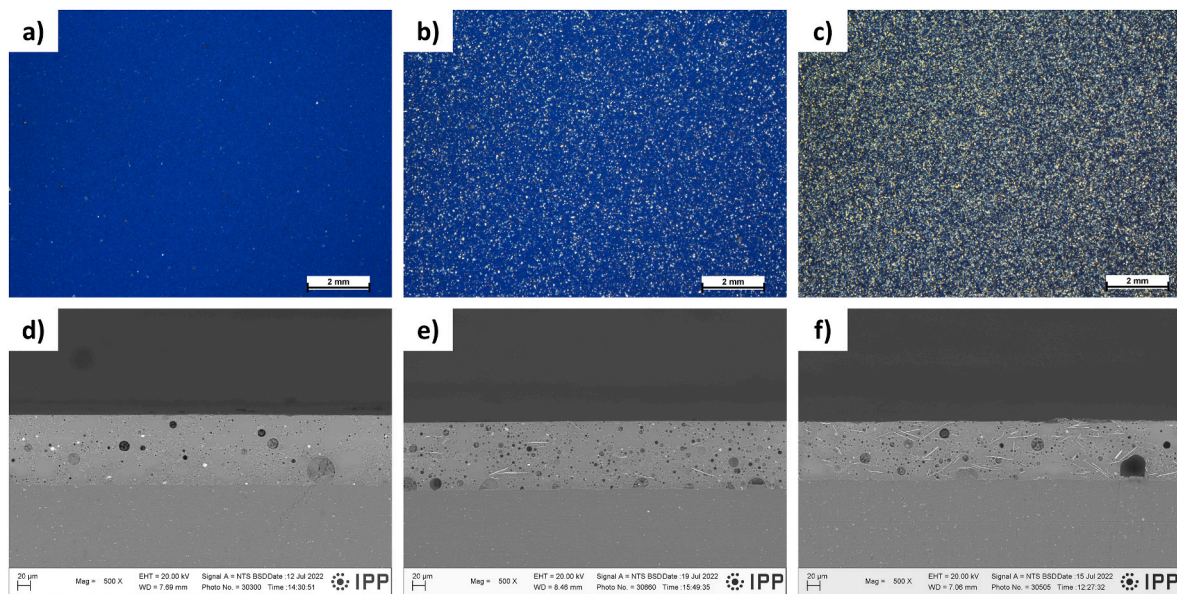| PARAMETER | REFERENCE | 1 % SS-F | 5 % SS-F |
|---|---|---|---|
| **Coating thickness (μm)** | 110 ± 4 | 119 ± 10 | 116 ± 8 |
| **Ra (μm)** | 0.17 ± 0.03 | 0.20 ± 0.03 | 1.06 ± 0.15 |
| **Porosity (%)** | 4.5 ± 2.1 | 8.3 ± 0.7 | 10.3 ± 2.0 |
| **Maximum pore Ø (μm)** | 33 ± 10 | 23 ± 5 | 31 ± 14 |

**Fig. 1.** In-plane optical (a–c) and cross-sectional SEM (d–f) micrographs of the samples under investigation.
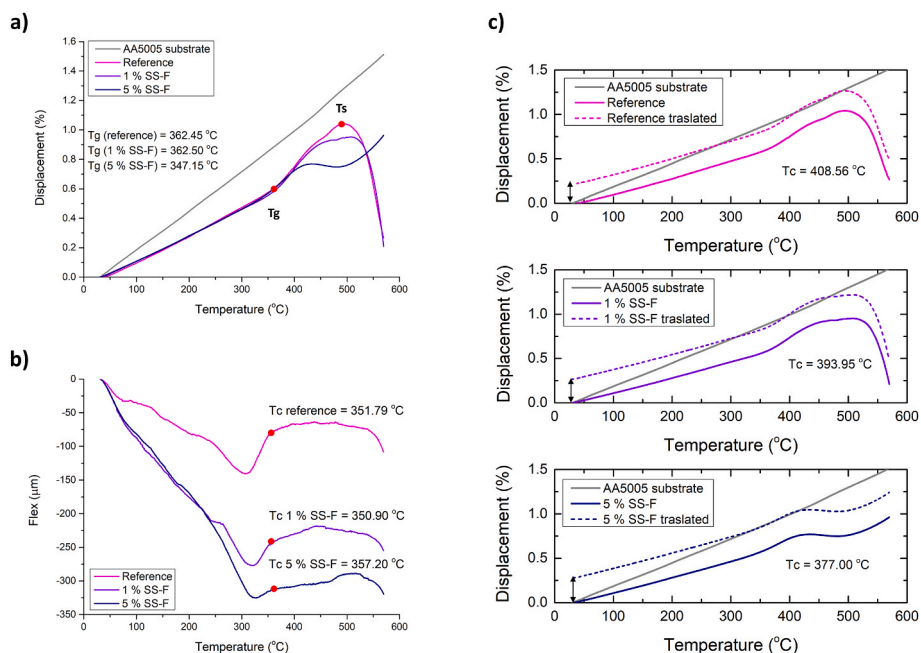


**Fig. 2.** Experimental assessment of residual stresses by thermal analysis: (a) dilatometric curves, (b) flexural curves, (c) experimental assessment of residual stress with coupling temperature Tc calculated by optical fleximeter measurements.

orientation, as they are produced as "non-leafing" pigments and for this reason they show good wetting ability in the medium they are incorporated in and a uniform distribution through all coating's thickness.

### 3.2. Experimental assessment of residual stresses in produced coatings

Fig. 2 shows the results of the thermal analyses carried out to assess residual stresses in the produced coatings. Fig. 2a displays the dilatometric curves of both the metallic substrate and different enamel formulations. The substrate exhibits a linear thermal expansion within the examined temperature range. In contrast, the enamel formulations deviate significantly from this linear trend. The reference and 1 % SS-F formulations initially show a linear trend up to approximately 360 °C, after which the curves experience an increase in slope until reaching a

maximum (494 °C and 512 °C, respectively), that corresponds to the softening temperature (Ts). Above this temperature, the slope of the curve reverses, as surface tension takes control of the shape and makes the edges of the sample to round off. The 5 % SS-F formulation follows a linear trend up to 347 °C, but then the curve undergoes subsequent contraction and expansion, that can be associated with the detachment of the enamel layer's ends from the substrate. In this case, the softening temperature is clearly shifted at temperatures higher than 569 °C. In conclusion, it is possible to evaluate the CTE of the different samples in the 100–300 °C temperature range: a CTE of $27 \times 10^{-6}$ K$^{-1}$, $19 \times 10^{-6}$ K$^{-1}$, $18 \times 10^{-6}$ K$^{-1}$, $18 \times 10^{-6}$ K$^{-1}$, was assessed for the substrate, reference, 1 % SS-F, and 5 % SS-F samples, respectively.

Fig. 2b shows the results of the optical fleximeter analyses. All the samples show a downward flexure until reaching a minimum, which

corresponds to the glass-transition temperature (Tg) and it is due to the largest difference in the expansion between the enamel and the substrate. Such a downturn is gradually more accentuated by the presence of stainless steel which causes variations in the elastic modulus of the enamel. Subsequently, the difference between the dilatometric curves of the enamel and metal decreases and the sample shows an upwards flexure, until reaching a plateau value. The coupling temperature (Tc) is identified as the temperature at which a rapid variation on the curve slope is presented. Further heating does not change the curve anymore, as the enamel is in the liquid state and stresses are completely relieved, although a slight decrease of the curve due to pyroplastic deformation of aluminum can be observed. The coupling temperature was extrapolated by the inflection of the fleximeter curves, and it was corrected by the ΔT assessed by comparing the differences in Tg of the dilatometric curves and flexural curves. These differences are connected to the different shape of the samples used in the two tests and their different positioning with respect to the thermocouple and are dependent on the thermal diffusivity of the formulation. The dilatometric curves of the enamel formulations and the metallic substrates were superimposed at the extrapolated Tc, and it was possible to assess the level of compression ($\Delta C_{40}$) at 40 °C, equal to 0.201 %, 0.253 %, and 0.262 % for the reference, 1 % SS-F, and 5 % SS-F formulations, respectively. The level of compression of the enamel with respect to the metal support increases with the concentration of metallic additive, although this increase is not linear with the additive's concentration.

**Table 3**

Failure strain (%) for the samples tested in three-point and four-point configurations.

| CONFIGURATION | SAMPLE | FAILURE STRAIN (%) |
|---|---|---|
| 3-PB | Reference | 0.33 ± 0.00 |
| | 1 % SS-F | 0.37 ± 0.02 |
| | 5 % SS-F | 0.39 ± 0.03 |
| 4-PB | Reference | 0.37 ± 0.04 |
| | 5 % SS-F | 0.48 ± 0.02 |

### 3.3. In-situ three-point and four-point flexural tests with microtest deben tensile tester

In-situ three-point and four-point mechanical tests coupled with SEM observations are useful to study the failure mechanisms of the different samples and to quantitative assess their resistance to cracking. In this context, it was possible to calculate the stress-strain curves, evaluate the evolution of the crack density together with the applied strain, and assess the failure strain (i.e. strain level at which is possible to observe the onset of damage). Crack density and failure strain were calculated by counting the transversal cracks visible in the sample's cross-section at 100× magnification. Four-point bending tests have been exploited on the reference and 5 % SS-F samples only to obtain additional information on the behavior of the samples when they are subjected to a uniform stress over a wider area.

Table 3 shows the failure strain values for the different samples taken under consideration.

The tensile yield stress was used to evaluate the elastic-plastic limit of stress-strain curves. The metallic substrate's elastic regime ended at a strain value of 0.18 ± 0.5 % and 0.21 ± 0.6 % for three-point and four-point bending setups, respectively, which is significantly less than for the coated samples (see Fig. 3). This implies that the coating failure consistently occurs when the substrate is significantly in the plastic regime. The samples tested in four-point bending configuration showed higher failure strains compared to the ones obtained from three-point bending tests. Specifically, the 5 % SS-F sample exhibited a 12 % increase compared to the reference for the three-point configuration, and a 30 % increase for the four-point configuration.

Fig. 3 shows the average stress-strain curves (Fig. 3a and c) and the evolution of the crack density (Fig. 3b and d) for the samples tested in three-point (Fig. 3a and b) and four-point bending (Fig. 3c and d) configurations.

The crack density evolution in the three-point bending configuration exhibits similar trends for all the formulations until a strain level of 0.7 %. Beyond this point, the composite samples undergo a slight inflection in the curve, but only the 5 % SS-F formulation shows a decreased crack density even at higher strain levels. To further understand the impact of stress distribution over a wider sample volume on the mechanical behavior of the coatings, the same tests were conducted on the extreme
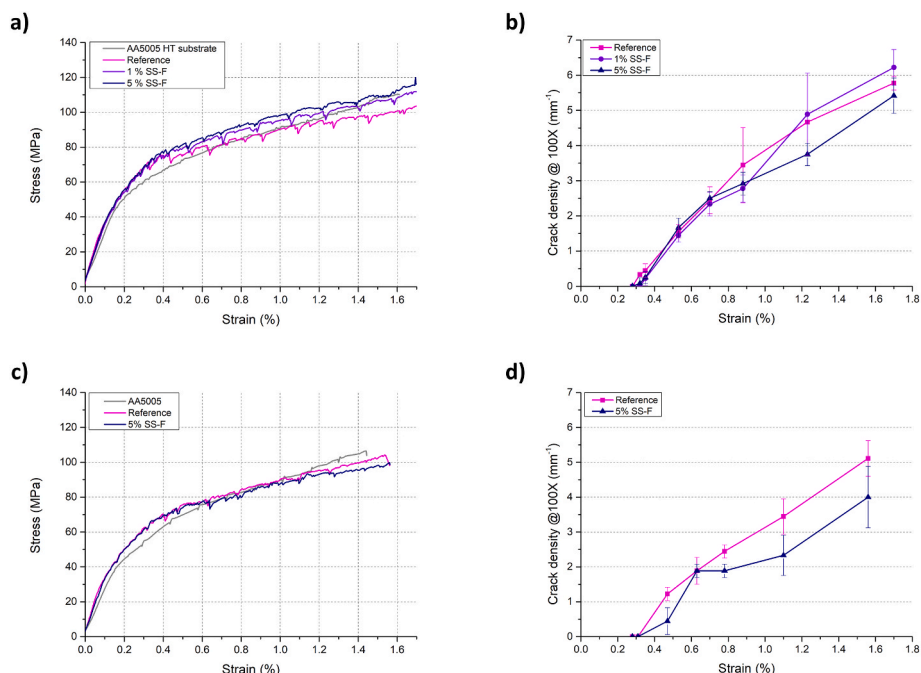


**Fig. 3.** Output results from three-point (a–b) and four point (c–d) bending tests with Microtest 200 N Deben tensile tester.
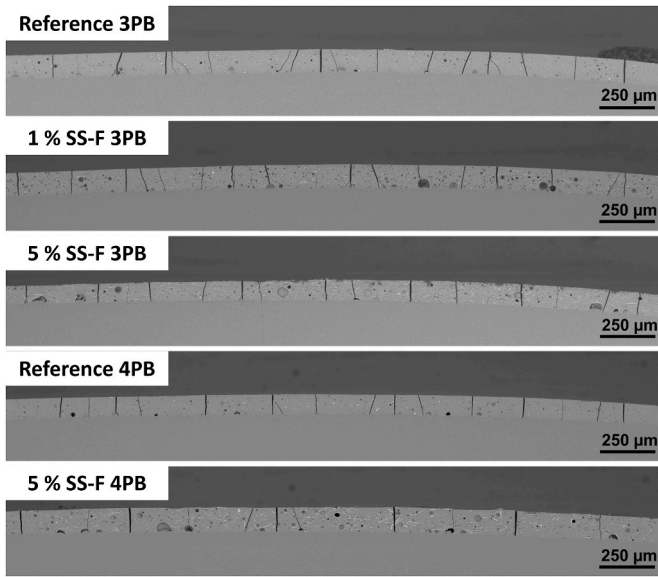
**Fig. 4.** Cross-sectional SEM images of the investigated samples tested in 3-point (a–c) and 4-point (d–e) bending configuration after 1.00 mm extension: a) reference, b) 1 % SS-F, c) 5 % SS-F, d) reference, e) 5 % SS-F.

formulations using the four-point bending configuration. The crack density evolution in these tests displays different trends for the three types of samples. In the four-point bending tests, both samples exhibit an initial abrupt crack onset stage until a strain of 0.6 %, but after this stage they starts behaving differently. The reference formulation undergoes a linear crack increase as the strain continues to rise, whereas the 5 SS-F% sample shows an intermediate plateau area (between 0.8 % and 1.0 % strain) followed by a new increase in the crack density value. These observations suggest that stress distribution and formulation composition significantly influence the evolution of crack density in different bending configurations, indicating varied mechanical behaviors for the coatings under different loading conditions: for 4 PB, i.e. setup with maximum loading between the whole area between central loading supports, the stainless-steel flakes are able to counteract both the nucleation (increase failure strain) and propagation of cracks (plateau

region at intermediate strain levels). In the case of 3 PB, where the maximum bending occurs only in the central section of the sample, only a small increase in the failure strain can be detected.

Fig. 4 provides a detailed view of the cross-sections after the 3-point and 4-point bending tests. The figure illustrates the propagation path of transversal cracks and their interaction with stainless steel flakes and internal pores. The cracks tend to preferentially propagate in correspondence with internal pores, sometimes shifting along the x-axis to reach interfacial pores. This effect becomes less pronounced as the concentration of the metallic additive (316L flakes) increases, as the interaction between the flakes and cracks becomes the dominant factor. Another important effect is the branching of cracks, which is evident in the reference sample and still present in the 1 % SS-F samples, but almost absent in the 5 % SS-F sample. The presence of the 316L flakes consistently leads to significant crack/flakes interaction phenomena, causing cracks to deviate and increasing the crack propagation path. Notably, no delamination phenomena are observed at the interface. Fig. 4 clearly highlights the difference in crack density between the reference sample and the 5 % SS-F sample, as well as between the 5 % SS-F samples tested in different configurations.

Fig. 5 shows some detailed SEM images of crack/flakes interaction phenomena after 1.00 mm displacement (end of test) in three-point bending configuration for the 1 % SS-F (Fig. 5a, b, 5c) and 5 % SS-F (Fig. 5d, e, 5f) samples. These details were acquired on the same samples that are shown in Fig. 4. Three main interaction mechanisms can be noticed: crack bridging (Fig. 5a and e), crack deflection (Fig. 5c), and additive plastic deformation/rupture (Fig. 5b, d, 5f), that is often combined with crack deflection.

### 3.4. In-situ AE test in four-point bending setup

Table 4 reports the activity analysis and the parametric analysis for the samples under study. The results are the average values of three tests on different samples. The substrate gives rise to a limited number of acoustic events having amplitudes lower than 50 dB: these events may arise from the elastic-plastic deformation of the substrate or friction events between the anvils and the substrate. Enamelled samples show an increased AE activity with respect to the substrate. The trend for the number of events is not definite, but it is necessary to consider relatively high scatter of the 1 % SS-F sample. Despite this fact, it is possible to state that in presence of 316L stainless steel flakes the number of events
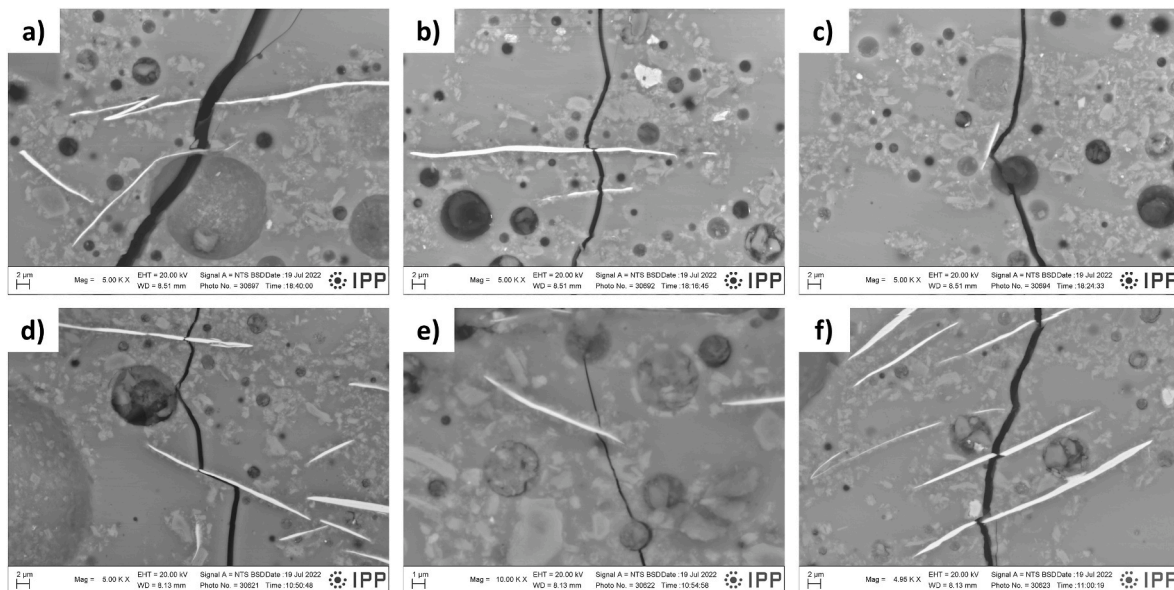


**Fig. 5.** Detailed cross-sectional SEM images of the investigated samples tested in 3-point bending configuration after 1.00 mm extension: a-c) 1 % SS-F sample, d-f) 5 % SS-F sample.

**Table 4**

Activity and parametric analysis for in-situ 4-point bending AE tests.

| Sample | Hits | AE average parameters | | | |
|---|---|---|---|---|---|
| | | Amplitude maximum (dB) | Amplitude average (dB) | Energy maximum (aJ) | Energy average (aJ) |
| **Substrate** | $36 \pm 3$ | $49 \pm 1$ | $42 \pm 0$ | $196 \pm 76$ | $29 \pm 12$ |
| **Reference** | $1157 \pm 206$ | $92 \pm 2$ | $48 \pm 1$ | $7.5 \times 10^6 \pm 2.0 \times 10^6$ | $4.7 \times 10^4 \pm 1.8 \times 10^4$ |
| **1 % SS-F** | $2584 \pm 856$ | $92 \pm 1$ | $48 \pm 0$ | $6.8 \times 10^6 \pm 1.8 \times 10^6$ | $3.0 \times 10^4 \pm 9.7 \times 10^4$ |
| **5 % SS-F** | $1796 \pm 378$ | $87 \pm 3$ | $50 \pm 1$ | $2.6 \times 10^6 \pm 1.3 \times 10^6$ | $1.1 \times 10^4 \pm 1.3 \times 10^4$ |

is increased when compared to the reference sample. Regarding maximum amplitude, all samples display transversal cracking, resulting in high amplitude and energy events. However, the 5 % SS-F sample shows a slight decrease in maximum registered amplitude. As for average amplitude, no noticeable differences are observed among the samples since the large number of events tends to balance the average amplitude. Interestingly, the presence of stainless-steel flakes appears to reduce both maximum and average energy of events during the four-point bending tests. This reduction may be attributed to the flakes' ability to absorb some energy through plastic deformation, thereby decreasing the magnitude of the acoustic events. The reduction of the average energy of the AE events is not linear with the concentration of the stainless-steel flakes, as in the case of the 1 % SS-F and 5 % SS-F samples it is possible to notice a reduction of 22 % and 54 % of the involved average energy, respectively.

Fig. 6 shows the evolution of AE events during the tests for four representative samples of the different formulations taken under consideration. The previous graph display the number of cumulative events and the amplitude of the registered events together with stress-time curves. Some differences can be noticed among the samples: the addition of 1 % stainless-steel flakes leads to an increase of acoustic events in the 55–70 dB region, whereas the presence of 5 % steel flakes leads to both a densification of events in the 55–70 dB region and a reduction of events in the 70–100 dB region. All these differences are particularly evident in the first 170 s of the test, that correspond to the area where plastic deformation of the substrate takes place as the first cracks develop in the coatings. These observations are highlighted by the histograms in Fig. 7. Fig. 7a reports the number of hit/amplitude histograms in all the tested interval (600 s) and the histograms of the events registered in the first 170 s of test (in grey superimposed). Fig. 7b shows the same graphs but in a more restricted amplitude range. The

cumulative number of AE represents the number of mechanical events that are generated during the test, but it does not give information about the magnitude of these events, that is well represented by the AE energy involved. Thus, it is possible to monitor the evolution of AE cumulative energy and identify the onset of mechanical damage as an abrupt increase in the cumulative energy parameter. Table 5 reports the cumulative energy registered in all the tests, the cumulative energy after 170 s (thus just after the elastic-plastic limit of the substrate), and strain at which damage starts to occur. The cumulative energy value is notably reduced for the 5 % SS-F samples, showing a decrease of 69 % and 66 % after 170s and 600s, respectively. A similar trend can be observed for the onset strain, with a reduction of about 78 % with respect to the reference sample.

## 4. Discussion

The mechanical properties of vitreous enamel coatings are greatly dependent on their microstructural features. Literature results of strain-to-failure flexural tests highlighted that the three variables most strongly affecting enamel coatings durability during mechanical testing are the residual stresses arising from the different thermal expansion coefficients among the metal and the enamel layer, the Young's modulus of the enamel coating, and its thickness. In addition to that, surface roughness and internal porosity (circularity and dimension of pores) should be considered as well [60].

The microstructural characteristics of the different enamel coatings examined in this study are outlined in Table 2. The thicknesses of the coatings are measured using a thickness gauge, and the measurements are comparable across the three sample series. Surface roughness is an important parameter to be considered, as high surface roughness can result from a high percentage of pores in the outer layers of the enamel
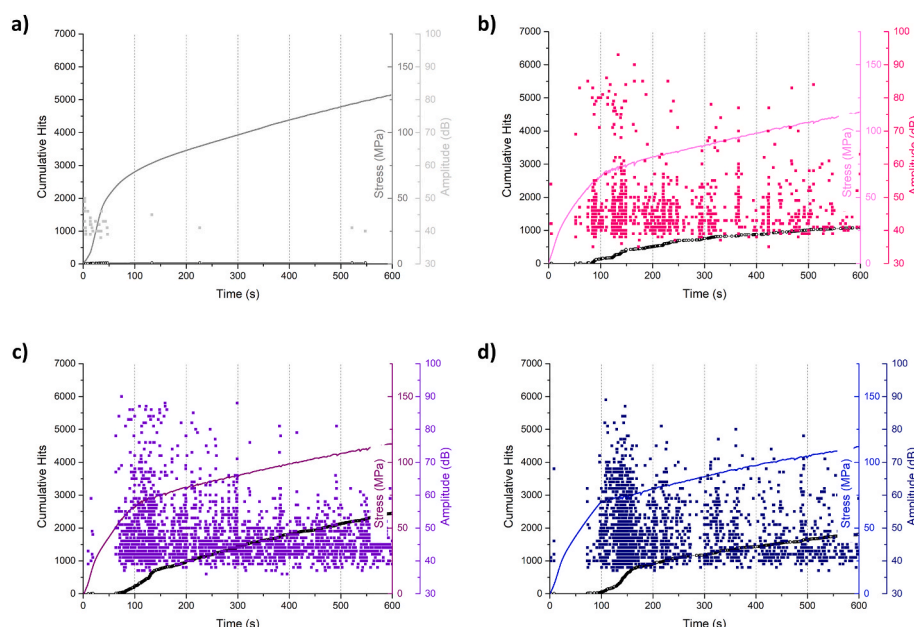


**Fig. 6.** AE activity/parametric overview of the samples tested in 4-point bending, a) metal substrate, b) reference, c) 1 % SS-F. d) 5 % SS-F.
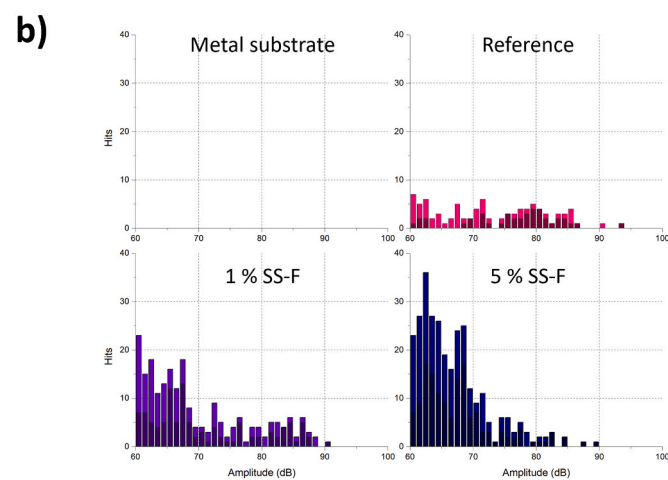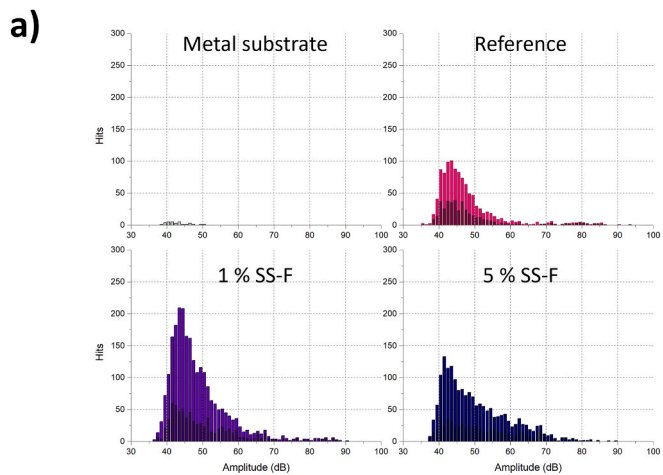
**Fig. 7.** Amplitude histogram of the AE tests performed in 4-point bending configuration, a) complete time interval (600s), b) 170s time interval.



**Fig. 8.** Correlation graph between the failure strain during three-point and four-point bending tests and the compressive residual stresses in the produced coatings.

coating, which can act as initiators for cracks. In this study, all enamel samples exhibit a uniform distribution of pores throughout the whole thickness of the enamel, and no preferential crack formation at superficial pores is observed. As regards the Young's modulus of the coatings no relevant differences can be observed (as shown by stress-strain curves in Fig. 3). Thus, residual stresses and internal porosity are the only parameters to be discussed.

Fig. 8 shows a brief overview of the main results obtained by this study.

First, it is important to highlight the correlation between the onset strain and the compressive residual stresses in the coatings. The 5 % SS-F sample shows an increased onset strain of about 18 % and 30 % with respect to the reference sample in the three-point and four-point bending configurations, respectively. At the same time, it is possible to highlight that the level of compression of the 5 % SS-F sample is 30 % higher with respect to the reference formulation. So then, the failure strain of the coatings seems to greatly depend on the residual stresses of the coatings
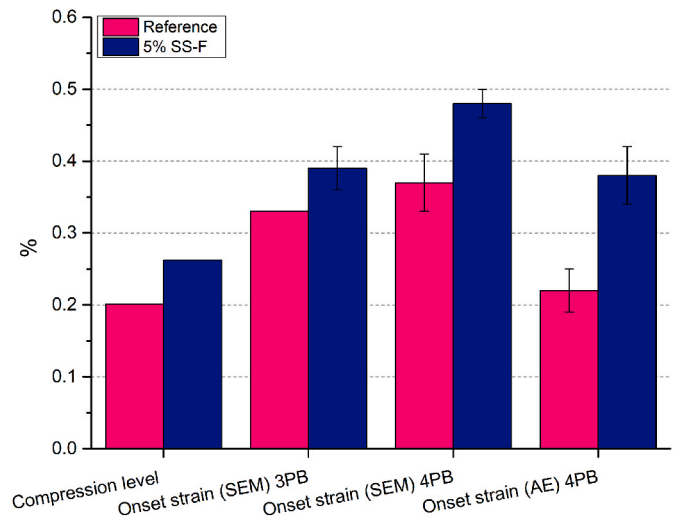
prior to testing, particularly when the samples are tested in four-point bending configuration. The addition of stainless-steel flakes inside the formulation is then able to modify the thermal properties of the formulation, leading to the creation of different compressive states, that are the direct cause of the delayed strain at which the first damaging event (propagating crack) can be noticed. The experimental assessment of the residual stresses is then useful to understand the cause of the different behaviour of the samples in terms of initialization of damage.

Porosity is another key aspect that could influence the onset strain at which damage occurs. Generally, it decreases by increasing the number of pores and their dimensions. Considering only the internal porosity, the samples should show a decreased failure onset strain with a higher 316L SS-Fs concentration (which correlated with higher porosity values), but the presence of internal compressive residual stresses overcome this negative aspect.

In-situ SEM observations are useful to evaluate the onset of damage, the evolution of crack density during the bending tests, and the additive-crack interaction mechanisms. Stainless-steel flakes counteract the propagation of cracks and the nucleation of new cracks at intermediate stress levels (0.6–1.1 %), particularly when the maximum momentum is homogeneously distributed over a wider area of the tested sample, as in 4 PB tests, rather in narrow section as in 3 PB setup. The main additive-crack interaction mechanisms are crack deflection, crack bridging, and plastic deformation of the additive.

The exploitation of in-situ SEM analyses is very time-demanding, whereas the use of the AE technique can provide valuable information on the studied systems by simple and quick measurements.

As a first thing, it is possible to notice an increased number of AE events with the higher concentration of metallic additive, presumably due to the many interaction phenomena occurring between the flakes and the advancing cracks. Acoustic events with amplitudes lower than 50 dB are due to the deformation of the metallic substrates, as already reported by literature studies [61], whereas high amplitudes events (85–100 dB) can be linked to the formation of through-thickness cracks

**Table 5**
Cumulative energy analysis for the samples tested in four-point bending configuration.

| Sample | Cumulative energy at 600s (aJ) | Cumulative energy at 170 s (aJ) | ε onset (%) |
|---|---|---|---|
| **Metal heat-treated** | $9.9 \times 10^2 \pm 3.0 \times 10^2$ | $8.4 \times 10^2 \pm 4.4 \times 10^2$ | – |
| **Reference** | $5.7 \times 10^7 \pm 3.1 \times 10^7$ | $4.1 \times 10^7 \pm 2.1 \times 10^7$ | $0.22 \pm 0.03$ |
| **1 % SS-F** | $7.3 \times 10^7 \pm 1.6 \times 10^7$ | $5.1 \times 10^7 \pm 6.2 \times 10^6$ | $0.25 \pm 0.02$ |
| **5 % SS-F** | $1.8 \times 10^7 \pm 4.2 \times 10^6$ | $1.4 \times 10^7 \pm 4.5 \times 10^6$ | $0.38 \pm 0.04$ |

[61], and they decrease in number with the presence of the metallic additive. The assignation of medium-amplitude events can be made as follows: AE events with 55–65 dB amplitude can be attributed to the formation of discontinuous cracks, as they can be detected for all the tested formulations [56], whereas events with 70–85 dB amplitude can be attributed to the additive-crack interaction, as their number increase with the concentration of the metallic additive.

Energy of acoustic events is a very reliable parameter in assessing the evolution of damage as it considers the magnitude of the events. In this study, substrate-related events have a maximum energy of about $10^4$ aJ, as reported in literature studies, whereas coatings-related events have energy up to $10^7$ aJ [61] and their maximum energy value is reduced with an increased additive concentration. The evolution of cumulative energy during AE tests is useful to assess the onset damage strain, as a rapid increase in the cumulative energy indicates the formation of transversal cracks [62,63]. In the present case, the onset strain of the 5 % SS-F sample is 78 % higher with respect to the reference sample. Thus, the addition of the 5 % SS flakes seems to be beneficial in delaying the initiation of catastrophic damaging (confirming data from the failure strain obtained by SEM in-situ analyses) and in reducing the energy involved in the damaging process.

Thus, the presence of 5 % SS-F seems to have a beneficial role in counteracting the nucleation and evolution of damage, particularly when the stress is distributed over a wider volume of the sample. By a quantitative point of view, both in-situ SEM observations and AE analyses confirm that the damaging of the enamel coatings starts after the initialization of the plastic deformation of the substrate. The AE technique is shown to have a higher sensibility, as the onset strains are shifted to lower values with respect to the ones obtained by SEM in-situ analyses, and the differences between the samples are greatly appreciable.

## 5. Conclusions

The main aim of this study was to characterize the mechanical properties of composite enamel coatings admixed with 316L stainless steel flakes. Additionally, the research aimed to assess the reliability of different in-situ techniques for evaluating these properties. The main conclusions of this study are as follows.

- The addition of 316L stainless steel flakes is beneficial in counteracting cracks evolution in vitreous enamel coatings, particularly at intermediate strain levels (0.6–1.0 %).
- The addition of different concentration of 316L flakes within the enamel matrix modifies the thermal properties of the coatings and affects the residual compressive stresses at the end of the production process.
- In-situ SEM analyses are effective in identifying the failure micromechanisms and the interaction phenomena between advancing cracks and the metallic additive. The main interaction phenomena observed are crack deflection, crack bridging, and additive plastic deformation and/or rupture.
- In-situ AE analyses offer valuable insights into the type of damaging events, onset strain, and energy evolution occurring during failure of enamel coatings.
- In-situ AE analyses represent a preferable technique for exploring the mechanical properties of composite enamel coatings due to their high sensitivity and ease of implementation.

## CRediT authorship contribution statement

**Francesca Russo:** Data curation, Formal analysis, Investigation, Methodology, Writing – original draft, Writing – review & editing. **Emiliano Rustighi:** Conceptualization, Methodology, Supervision, Validation, Writing – review & editing. **Radek Muśálek:** Conceptualization, Methodology, Supervision, Validation, Writing – review &

editing. **Tomáš Tesař:** Investigation, Methodology, Writing – review & editing. **Vigilio Fontanari:** Conceptualization, Project administration, Supervision, Validation, Writing – review & editing. **Stefano Rossi:** Funding acquisition, Project administration, Supervision, Writing – review & editing.

## Declaration of competing interest

The authors declare that they have no known competing financial interests or personal relationships that could have appeared to influence the work reported in this paper.

## References

[1] J. Rödel, A.B.N. Kounga, M. Weissenberger-Eibl, D. Koch, A. Bierwisch, W. Rossner, M.J. Hoffmann, R. Danzer, G. Schneider, Development of a roadmap for advanced ceramics: 2010–2025, J. Eur. Ceram. Soc. 29 (2009) 1549–1560.
[2] J.S. Pelz, N. Ku, M.A. Meyers, L.R. Vargas-Gonzalez, Additive manufacturing of structural ceramics: a historical perspective, J. Mater. Res. Technol. 5 (2021) 670–695.
[3] N.P. Padture, Advanced structural ceramics in aerospace propulsion, Nat. Mater. 15 (2016) 804–809.
[4] X. Lv, F. Ye, L. Cheng, L. Zhang, Novel processing strategy and challenges on whisker-reinforced ceramic matrix composites, Compos. – A: Appl. Sci. 158 (2022) 106974.
[5] R.O. Ritchie, Toughening materials: enhancing resistance to fracture, Phil. Trans. R. 379 (2021) 20200437.
[6] M. Kotoul, J. Pokluda, P. Šandera, I. Dlouhý, Z. Chlup, A.R. Boccaccini, Toughening effects quantification in glass matrix composite reinforced by alumina platelets, Acta Mater. 56 (2008) 2908–2918.
[7] K.M. Prewo, J.J. Brennan, High-strength silicon carbide fibre-reinforced glass-matrix composites, J. Mater. Sci. 15 (1980) 463–468.
[8] A. Aramian, N. Razavi, Z. Sadeghian, F. Berto, A review of additive manufacturing of cermets, Addit. Manuf. 33 (2020) 101130.
[9] A.J. Ruys, 1 - introduction to metal-reinforced ceramics, in: A.J. Ruys (Ed.), Metal-Reinforced Ceramics, Woodhead Publishing, 2021, pp. 1–20.
[10] J.A. Yeomans, Ductile particle ceramic matrix composites— scientific curiosities or engineering materials? J. Eur. Ceram. Soc. 28 (2008) 1543–1550.
[11] Y. Ji, J.A. Yeomans, Microstructure and mechanical properties of chromium and chromium/nickel particulate reinforced alumina ceramics, J. Mater. Sci. 37 (2002) 5229–5236.
[12] G. de Portu, S. Guicciardi, C. Melandri, F. Monteverde, Wear behaviour of Al2O3–Mo and Al2O3–Nb composites, Wear 262 (2007) 1346–1352.
[13] M. Chmielewski, K. Pietrzak, Processing, microstructure and mechanical properties of Al2O3–Cr nanocomposites, J. Eur. Ceram. Soc. 27 (2007) 1273–1279.
[14] T. Isobe, K. Daimon, T. Sato, T. Matsubara, Y. Hikichi, T. Ota, Spark plasma sintering technique for reaction sintering of Al2O3/Ni nanocomposite and its mechanical properties, Ceram. Int. 34 (2008) 213–217.
[15] W.-H. Tuan, Y.-P. Pai, Mechanical properties of Al2O3-NiAl composites, J. Am. Ceram. Soc. 82 (1999) 1624–1626.
[16] V. Imbeni, I.M. Hutchings, M.J.W. Breslin, Abrasive wear behaviour of an Al2O3–Al co-continuous composite, Wear 233 (1999) 462–467.
[17] X. Lu, J. Li, X. Chen, C. Ran, Y. Wang, B. Liu, Y. Liu, M. Rashad, F. Pan, Grinding mechanism and mechanical properties of the in-situ synthesized Al2O3/TiAl composites, Ceram. Int. 45 (2019) 12113–12121.
[18] Y.-e. Qi, Y.-S. Zhang, L.-T. Hu, High-temperature self-lubricated properties of Al2O3/Mo laminated composites, Wear 280–281 (2012) 1–4.
[19] A. Smirnov, J.F. Bartolomé, Mechanical properties and fatigue life of ZrO2–Ta composites prepared by hot pressing, J. Eur. Ceram. Soc. 32 (2012) 3899–3904.
[20] Q. Chang, D.L. Chen, H.Q. Ru, X.Y. Yue, L. Yu, C.P. Zhang, Toughening mechanisms in iron-containing hydroxyapatite/titanium composites, Biomater 31 (2010) 1493–1501.
[21] E. Bernardo, G. Scarinci, A. Maddalena, S. Hreglich, Development and mechanical properties of metal–particulate glass matrix composites from recycled glasses, Compos. -A: Appl. Sci. 35 (2004) 17–22.
[22] Y. Waku, M. Suzuki, Y. Oda, Y. Kohtoku, Improving the fracture toughness of MgO–Al2O3–SiO2 glass/molybdenum composites by the microdispersion of flaky molybdenum particles, J. Mater. Sci. 32 (1997) 4549–4557.
[23] I. Dlouhy, A.R. Boccaccini, Preparation, microstructure and mechanical properties of metal-particulate/glass-matrix composites, Compos. Sci. Technol. 56 (1996) 1415–1424.
[24] G. Banuprakash, V. Katyal, V.S.R. Murthy, G.S. Murty, Mechanical behaviour of borosilicate glass-copper composites, Compos. -A: Appl. Sci. 28 (1997) 861–867.

[25] M. Chen, S. Zhu, M. Shen, F. Wang, Y. Niu, Effect of NiCrAlY platelets inclusion on the mechanical and thermal shock properties of glass matrix composites, Mater. Sci. Eng. 528 (2011) 1360–1366.

[26] E. Scrinzi, S. Rossi, The aesthetic and functional properties of enamel coatings on steel, Mater. Des. 31 (2010) 4138–4146.

[27] S. Rossi, F. Russo, M. Calovi, Durability of vitreous enamel coatings and their resistance to abrasion, chemicals, and corrosion: a review, J. Coating Technol. Res. 18 (2021) 39–52.

[28] L. Fan, F. Tang, G. Chen, S.T. Reis, M.L. Koenigstein, Corrosion resistances of steel pipe coated with two types of enamel by two coating processes, J. Mater. Eng. Perform. 27 (2018) 5341–5349.

[29] F. Tang, G. Chen, J.S. Volz, R.K. Brow, M. Koenigstein, Microstructure and corrosion resistance of enamel coatings applied to smooth reinforcing steel, Construct. Build. Mater. 35 (2012) 376–384.

[30] H. Qian, Z. Xu, S. Chen, Y. Liu, D. Yan, Silicon carbide/enamel composite coatings for steel corrosion protection: microstructure, thermal expansion behavior, and anti-corrosion performance, Surf. Coat. Technol. 434 (2022) 128172.

[31] H. Qian, S. Chen, T. Wang, G. Cheng, X. Chen, Z. Xu, Q. Zeng, Y. Liu, D. Yan, Silicon nitride modified enamel coatings enable high thermal shock and corrosion resistances for steel protection, Surf. Coat. Technol. 421 (2021) 127474.

[32] S. Rossi, F. Russo, M. Calovi, M. Del Rincon, D. Velez, The influence of the size of corundum particles on the properties of chemically resistant porcelain enamels, Ceram. Int. 47 (2021) 11618–11627.

[33] S. Rossi, L. Bergamo, V. Fontanari, Fire resistance and mechanical properties of enamelled aluminium foam, Mater. Des. 132 (2017) 129–137.

[34] F. Russo, V. Fontanari, S. Rossi, Abrasion behavior and functional properties of composite vitreous enamel coatings fabricated with the addition of 316L stainless steel flakes, Ceram. Int. 48 (2022) 23666–23677.

[35] Y. Liao, B. Zhang, M. Chen, M. Feng, J. Wang, S. Zhu, F. Wang, Self-healing metal-enamel composite coating and its protection for TiAl alloy against oxidation under thermal shock in NaCl solution, Corrosion Sci. 167 (2020) 108526.

[36] F. Wang, Y. Liu, Mechanical and tribological properties of ceramic-matrix friction materials with steel fiber and mullite fiber, Mater. Des. 57 (2014) 449–455.

[37] F. Pernot, R. Rogier, Mechanical properties of phosphate glass-ceramic-316 L stainless steel composites, J. Mater. Sci. 28 (1993) 6676–6682.

[38] M. Imbaby, K. Jiang, Net shape fabrication of stainless steel–alumina composite micro parts, J. Micromech. Microeng. 19 (2009) 045018.

[39] F. Russo, V. Fontanari, E. Rustighi, M. Lekka, L. Hernandez, S. Rossi, Composite vitreous enamel coatings with the addition of 316L stainless steel flakes: novel insights on their behaviour under mechanical stresses, Surf. Coat. Technol. 459 (2023) 129393.

[40] M. Zawischa, S. Makowski, M. Kuczyk, V. Weihnacht, Comparison of fracture properties of different amorphous carbon coatings using the scratch test and indentation failure method, Surf. Coat. Technol. 435 (2022) 128247.

[41] A.J. Ruys, 3 - fracture mechanics and design principles for metal-reinforced ceramics, in: A.J. Ruys (Ed.), Metal-Reinforced Ceramics, Woodhead Publishing, 2021, pp. 45–67.

[42] D.G. Eitzen, H.N.G. Wadley, Acoustic emission: etsablishing the fundamentals, J. Res. Natl. Bur. Stand. 89 (1984) 75–100.

[43] S. Gholizadeh, A review of non-destructive testing methods of composite materials, Procedia Struct. Integr. 1 (2016) 50–57.

[44] C.R. Ríos-Soberanis, Acoustic emission technique, an overview as a characterization tool in materials science, J. Appl. Res. Technol. 9 (2011) 367–379.

[45] A. Bendaoued, A. Zahrouni, M. Messaoud, O. Harzallah, S. Bistac, R. Salhi, Understanding the effect of nanoparticles TiO2, Al2O3 and SiO2 on damage mechanisms of a polymer composite, Ceram. Int. 49 (2023) 4160–4167.

[46] K. Hamdi, G. Moreau, Z. Aboura, Digital image correlation, acoustic emission and in-situ microscopy in order to understand composite compression damage behavior, Compos. Struct. 258 (2021) 113424.

[47] W. Li, G. Palardy, Damage monitoring methods for fiber-reinforced polymer joints: a review, Compos. Struct. 299 (2022) 116043.

[48] M. Saeedifar, D. Zarouchas, Damage characterization of laminated composites using acoustic emission: a review, Compos. B Eng. 195 (2020) 108039.

[49] G.N. Morscher, Z. Han, Damage determination in ceramic composites subject to tensile fatigue using acoustic emission, Materials 11 (2018) 2477.

[50] B. Swaminathan, N.R. McCarthy, A.S. Almansour, K. Sevener, A.K. Musaffar, T. M. Pollock, J.D. Kiser, S. Daly, Interpreting acoustic energy emission in SiC/SiC minicomposites through modeling of fracture surface areas, J. Eur. Ceram. Soc. 41 (2021) 6883–6893.

[51] F. Wang, X. Teng, X. Hu, Y. Jiang, X. Guo, L. Li, X. Liu, X. Liu, H. Lu, Damage and failure analysis of a SiCf/SiC ceramic matrix composite using digital image correlation and acoustic emission, Ceram. Int. 48 (2022) 4699–4709.

[52] E. Maillet, A. Singhal, A. Hilmas, Y. Gao, Y. Zhou, G. Henson, G. Wilson, Combining in-situ synchrotron X-ray microtomography and acoustic emission to characterize damage evolution in ceramic matrix composites, J. Eur. Ceram. Soc. 39 (2019) 3546–3556.

[53] D.V. Chernov, V.M. Matyunin, V.A. Barat, A.Y. Marchenkov, S.V. Elizarov, Investigation of acoustic emission in low-carbon steels during development of fatigue cracks, Russ. J. Nondestr. Test. 54 (2018) 638–647.

[54] A. Shanyavskiy, M. Banov, Acoustic emission methods for lifetime estimations in aircraft structures, Theor. Appl. Fract. Mech. 109 (2020) 102719.

[55] J.P. McCrory, A. Vinogradov, M.R. Pearson, R. Pullin, K.M. Holford, Acoustic emission monitoring of metals, in: C.U. Grosse, M. Ohtsu, D.G. Aggelis, T. Shiotani (Eds.), Acoustic Emission Testing, Springer, 2022, pp. 529–565.

[56] J.M. Miguel, J.M. Guilemany, B.G. Mellor, Y.M. Xu, Acoustic emission study on WC–Co thermal sprayed coatings, Mater. Sci. Eng. 352 (2003) 55–63.

[57] A.I. Andrews, S. Pagliuca, Porcelain Vitreous Enamels and Industrial Enamelling Processes, third ed., International Enamellers Institute and Porcelain Enamel Institute, 2011.

[58] J.L. Amorós, A. Blasco, J.V. Carceller, V. Sanz, Acuerdo esmalte-soporte (II) expansion termica de soportes y esmaltes ceramicos, Tecnica Ceramica 179 (1997) 644–657.

[59] F.G. Franceschini, O.R. Klegues Montedo, S. Arcaro, C.P. Bergmann, Aluminum borophosphate glaze-coated aluminum alloy substrate: coating properties and coating/substrate coupling, Ceram. Int. 47 (2021) 2050–2057.

[60] L. Rossetti, V. Dal Re, A. Zucchelli, Mechanical behaviour of functionally graded composite vitreous enamelled steel sheets, Mater. Sci. Forum 636–637 (2010) 1483–1489.

[61] D. Dalmas, S. Benmedhakène, H. Kébir, C. Richard, A. Laksimi, J.M. Roleandt, Investigation of failure mechanisms in WC–Co coated materials, Surf. Coat. Technol. 173 (2003) 130–143.

[62] M. Surgeon, E. Vanswijgenhoven, M. Wevers, O. Van Der Biest, Acoustic emission during tensile testing of SiC-fibre-reinforced BMAS glass-ceramic composites, Compos.-A: Appl. Sci. 28 (1997) 473–480.

[63] J. Voyer, F. Gitzhofer, M.I. Boulos, Study of the performance of TBC under thermal cycling conditions using an acoustic emission rig, J. Therm. Spray Technol. 7 (1998) 181–190.